



Review

A Review on the Effects of ZnO Nanowire Morphology on the Performance of Interpenetrating Bulk Heterojunction Quantum Dot Solar Cells

Meibo Xing, Longxiang Wang and Ruixiang Wang *

Beijing Engineering Research Centre of Sustainable Energy and Buildings, School of Environment and Energy Engineering, Beijing University of Civil Engineering and Architecture, Beijing 100044, China; xingmeibo@bucea.edu.cn (M.X.); wlx8611@163.com (L.W.)

* Correspondence: wangruixiang@bucea.edu.cn; Tel.: +86-29-82668738; Fax: +86-29-82668725

Abstract: Interpenetrating bulk heterojunction (IBHJ) quantum dot solar cells (QDSCs) offer a direct pathway for electrical contacts to overcome the trade-off between light absorption and carrier extraction. However, their complex three-dimensional structure creates higher requirements for the optimization of their design due to their more difficult interface defect states control, more complex light capture mechanism, and more advanced QD deposition technology. ZnO nanowire (NW) has been widely used as the electron transport layer (ETL) for this structure. Hence, the optimization of the ZnO NW morphology (such as density, length, and surface defects) is the key to improving the photoelectric performance of these SCs. In this study, the morphology control principles of ZnO NW for different synthetic methods are discussed. Furthermore, the effects of the density and length of the NW on the collection of photocarriers and their light capture effects are investigated. It is indicated that the NW spacing determines the transverse collection of electrons, while the length of the NW and the thickness of the SC often affect the longitudinal collection of holes. Finally, the optimization strategies for the geometrical morphology of and defect passivation in ZnO NWs are proposed to improve the efficiency of IBHJ QDSCs.

Keywords: interpenetrating bulk heterojunction; quantum dot solar cells; ZnO nanowire; synthetic method; geometric optimization; defect passivation



Citation: Xing, M.; Wang, L.; Wang, R. A Review on the Effects of ZnO Nanowire Morphology on the Performance of Interpenetrating Bulk Heterojunction Quantum Dot Solar Cells. *Nanomaterials* **2022**, *12*, 114. <https://doi.org/10.3390/nano12010114>

Academic Editor: Seok-In Na

Received: 23 November 2021

Accepted: 27 December 2021

Published: 30 December 2021

Publisher's Note: MDPI stays neutral with regard to jurisdictional claims in published maps and institutional affiliations.



Copyright: © 2021 by the authors. Licensee MDPI, Basel, Switzerland. This article is an open access article distributed under the terms and conditions of the Creative Commons Attribution (CC BY) license (<https://creativecommons.org/licenses/by/4.0/>).

1. Introduction

The world environmental and energy crisis calls for the imminent development of renewable or nonconventional energies. As the most abundant source of clean energy on the planet, solar energy is an important approach to achieving the goal of carbon neutrality in the future [1]. To date, three generations of solar cells have been evolved to harvest solar energy as efficiently as possible [2], but they are still fundamentally limited in terms of solar cell efficiency, including thermalization losses from the absorption of high-energy photons, the non-absorption of low-energy photons, extraction losses due to unavoidable charge carrier recombination, and other mechanisms of energy loss [3].

Quantum dot solar cells offer the advantage of a zero-dimensional structure [4]. Due to their remarkable multiple exciton generation [5,6], hot carrier effect [7], possible intermediate band cell structure [8–10], and multi-junction cell structure [11,12], QDSCs offer the real possibility of boosting energy conversion efficiency beyond the Shockley and Queisser (SQ) limit of 32% for traditional silicon-based SCs [13]. In the past few decades, QDs have been widely researched and integrated in various kinds of SCs, such as Schottky junction colloidal quantum dot (CQD) SCs [14,15], depleted heterojunction CQDSCs [16–18], quantum junction CQDSCs [19–21], and quantum dot-sensitized solar cells (QDSSCs) [22–24]. However, the PbS QDSCs that have been widely studied have only reached a record efficiency of 13.3% [25], which is far from the theoretical efficiency of 45% for a single-junction

solar cell [26]. The main reason for this situation is that various sub-band gap trap states could be introduced in the synthesis and ligand exchange processes of CQD materials. QDSCs are still limited by the trade-off between carrier extraction and light absorption. A typical planar n-p-p⁺-type PbS QDSC usually features an absorption layer that is only about 300 nm thick, while a thickness of QD film of about 1 μm is required to achieve the full absorption of solar radiation. Generally, limited carrier diffusion length (L_D) and depletion width (W_D) are the main factors limiting the thickness of the absorption layer [27]. Thus, maximizing the recombination lifetimes of both charge carriers and their transport properties, which are related to L_D and W_D , is essential to achieve further advances in the thickness of the absorption layer. The IBHJ structure is considered to be another effective solution. IBHJ QDSCs feature a driving force to separate and transport the carriers with band bending and, at the same time, orthogonalize the direction of light absorption and electron–hole pair (EHP) separation, so that the absorber layer is thick enough to produce photocarriers that can be utilized [18]. Their n-type metal oxide acceptor is composed of 1D NWs (usually TiO₂ or ZnO; here, we mainly focus on ZnO, since it easily synthesizes various nanostructures and offers higher electron mobility than TiO₂). Simulation studies have shown that compared with planar solar cells, this type of cell structure is particularly advantageous when the optical absorption depth is comparable to the thickness of the device and the rate of carrier recombination in the depletion region is relatively large [28,29]. In addition, 3D structures have been shown to reduce surface optical reflection and enhance the absorption efficiency of SCs [30,31]. Moreover, the bending durability of ZnO NW arrays may offer promising prospects to meet the demands of flexible photovoltaic devices. Under bending conditions, interpenetrating structures can effectively release stress and thus resist the performance degradation caused by bending better than comparable planar devices [32]. Recently, a record short-circuit current density (J_{SC}) of 33.2 mA cm⁻² with a power conversion efficiency (PCE) of 10.62% was demonstrated for a PbS IBHJ QDSC employing the luminescence down-shifting method [33]. Further improvements of device performance require fine control of the morphology of NWs. For instance, in a piezoelectric strain sensor, inclined nanowires respond well to vertical contact forces, while vertically aligned nanowires are more sensitive to surface flow [34]. In IBHJ QDSCs, a better vertical arrangement of NWs can prevent the formation of large voids during the deposition of QDs [35]; the density, length, and surface defects of NWs directly affect the final performance of SCs. Besides, in real-world applications, different synthesis methods often feature different levels of morphology control precision, and the synthesis method must be considered to adapt to the application system of QDSC mass production. Therefore, it is necessary to review the preparation process of NW and analyze the morphology optimization mechanism of NWs.

In this study, several synthesis methods of ZnO NW are briefly introduced, ranging from vapor-phase methods and laser interference lithography to solution-based synthesis methods. The morphology control of hydrothermal-grown NW is mainly discussed, since hydrothermal (HT) method is simple, easy to operate, and suitable for large-scale application. Next, the effects of the geometrical morphology for the HT-grown ZnO NW on the performance of SCs is surveyed. Finally, the optimization strategies of NW morphology are discussed. Subsequently, the relationship between the process of photocarrier collection (electron transverse collection and hole longitudinal collection) and the morphology of NW is analyzed, and the control of the morphology of NW is proposed. In terms of interface optimization, the current strategies for the passivation of NW surface defects are summarized.

2. Preparation of ZnO Nanowires

Recently, ZnO NWs have gained considerable attention from the academic community for the fabrication of QD solar cells [36]. A variety of bottom-up approaches, including evaporation/chemical vapor deposition [37,38], solution-based synthesis methods (hydrothermal, electrodeposition) [39], and pulsed laser deposition (PLD) [40] has been exploited for the synthesis of ZnO NWs. Other growth methods, such as flame transport approach [41], electrospinning [42], molecular beam epitaxy (MBE) [43] etc., are also possible. Methods of controlling NW morphology by chemical vapor deposition and laser interference lithography are briefly introduced in the review, and then the hydrothermal method is mainly focused on, since it is simple and cheap.

2.1. Chemical Vapor Deposition

Typically, chemical vapor deposition (CVD) for the fabrication of ZnO NWs is carried out in a tubular furnace, as shown in Figure 1. The quartz boat with the Zn source and Si substrate were placed at the center of quartz tube, which was placed inside a tube furnace [44]. Generally, the formation of different diameters and lengths can be achieved by adjusting the flow rate of the carrier gas and the pressure during growth. In an experiment using argon as the carrier gas, the length and diameter of the NWs increase with the rise of oxygen supply. A further increase in the carrier gas flow rate triggers turbulent flow in the mixing process of the carrier gas and zinc vapor, and irregular results tend to occur [44]. Bhutto et al. [45] found that the final product was very short NWs, or even a layer of thin film at a low zinc vapor pressure, while the NWs grew with good orientation and uniform density at an appropriate vapor pressure. The condition of the substrate is another factor in the growth of aligned NW arrays. Well-aligned and uniform ZnO NW growth requires epitaxy, and the deposition of a c-oriented polycrystalline seed layer on a non-epitaxial substrate is an economical and versatile route [46]. Li et al. [47] found that the density of NWs increased and the degree of vertical arrangement improved with the increase in the seed layer thickness. Other studies have shown that the different deposition temperature and deposition methods of the ZnO seed layer also affect the orientation, morphology, and crystal quality of ZnO NWs grown by vapor deposition [47,48]. Furthermore, the metal catalysts in the vapor–solid–solid growth method are also important factors [49]. For example, neighboring metal catalysts may coalesce into larger-sized islands, leading to inferior control over the nanowire position and density when they are located at the semiconducting substrate during NW growth [50].

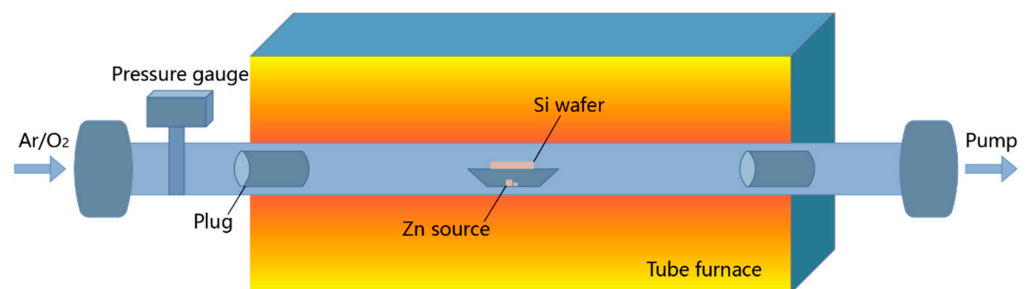


Figure 1. Schematic of CVD system used for the growth of ZnO NWs [44].

2.2. Laser Interference Lithography

The optical lithography and laser interference lithography (LIL) techniques, combining chemical and physical etching techniques to form patterned geometry, are more precisely designed and controllable methods used in the fabrication of ZnO nanostructures [51]. The LIL technique is based on the interference of two coherent light beams to form a horizontal standing wave pattern, which is applied to expose and record the patterns of periodic nanodot arrays (generally spin-coated onto a c-oriented ZnO seed layer) on the photoresist [52]. Wei et al. [53] demonstrated an approach to the patterned growth

of ZnO NW arrays by combining the LIL and hydrothermal (HT) growth methods. The epoxy-based negative photoresist SU-8 was spin-coated onto a 2-inch silicon or sapphire wafer with a (0001) surface-oriented ZnO layer above it. A uniform pattern of open-hole arrays was formed at the unexposed locations of the SU-8 layer after two consecutive laser exposures. Next, the substrate with a patterned SU-8 layer was placed facing downward into the growth solution for the growth of ZnO NWs, as shown in Figure 2 [53]. In this way, the diameter, spacing, and length of the NWs can be well controlled.

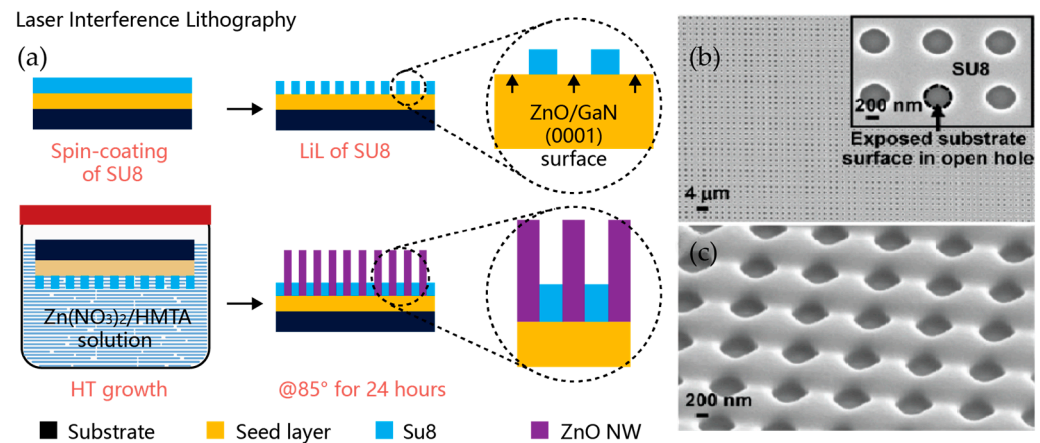


Figure 2. Schematics of the manufacturing process of ZnO NW arrays using laser interference techniques: (a) Fabrication process using the LIL approach for large-scale patterned ZnO NW arrays; (b) scanning electron microscope (SEM) image of patterned SU-8 film; (c) SEM image of patterned photoresist film [53].

2.3. Hydrothermal Method

Compared with other synthetic methods, the HT method has received widespread attention due to its advantages, including its low cost, low temperature, high yield, good expansibility, easy processing, and the flexibility it offers in the choice of both the synthesis pattern and the initial components (precursors and additives) [34,54,55]. The morphology and properties of ZnO NWs can be controlled by changing the growth parameters [56,57]. Generally, increasing the growth time causes the nanowires' aspect ratio to increase gradually, which is attributed to the fact that the axial growth rate is higher than the lateral growth rate [58,59]. Muchuweni et al. [60] observed improved crystallinity and poorly aligned NWs with increasing growth time. The length and diameter of the ZnO NWs vary with the concentration of growth solution; a higher concentration yields a larger length and diameter [61]. Amin et al. [57] observed the change from NWs to nanopillars and finally polycrystalline thin films upon changing from lower concentrations (<25 mM) to higher concentrations (>400 mM). In a similar study, Gerbreder et al. [62] concluded that the minimum concentration value is 25 mM; concentrations lower than this would lead to incomplete nanorod formation with chaotic orientations since the solutions would be depleted too quickly. Consistent with the effect of solution concentration, higher temperatures enhance the driving force of the chemical reaction, giving rise to high-aspect-ratio NWs [58]. The ZnO NW is homogeneous and well-arranged under 90 °C, which is considered to be the optimal temperature in many articles [62]. The pH value is another important factor. Redundant OH[−] ions suppress the influence of the competition mechanism, hence the difference in growth rate in the different directions [62,63]. When the pH value of the solution is reduced, the acidic environment may etch the seed layer and thus reduce the density of the NWs, while on the other hand, abundant Zn²⁺ results in the growth of ZnO NWs with larger lengths and diameters [56,57]. However, the growth of NWs is not observed at a low pH value (pH < 4.6 in the research of Amin et al. [57]). This behavior is probably attributable to the absence of hydroxide complexes (Zn(OH)_n), which are essential for the growth of ZnO NWs [64].

As in the CVD method, substrate properties also play an important role. The effects of surface energy and seed layer annealing conditions on seed layer growth and HT-grown ZnO NWs were investigated by changing different conditions in the research of Park et al. [65], as shown in Figure 3a. Demes et al. [66] investigated the relationships between the characteristics of grown NWs and (i) the structural properties and morphologies of ZnO films (mean grain size (MGS), texture coefficient, and surface coverage rate) and (ii) growth duration time (t) in detail. The growth process of the NWs is shown in the Figure 3b. Specifically, the growth of the NWs starts from the nucleation site, with an initial diameter d_0 at the seed layer surface, before proceeding along the lateral as well as the vertical direction at a rate of V_{lat} and V_{long} , respectively. According to the authors' observations, the main parameter influencing the NW aspect ratio and dimension appears to be the mean grain size of seed layers, while the texture coefficient of the seed layer can greatly influence the NW density [66]. In addition, the morphological properties of NWs grown using the HT method can also be optimized by postprocessing. Here, we briefly summarize the dominant factors affecting the morphology of hydrothermally grown NWs (see Table 1).

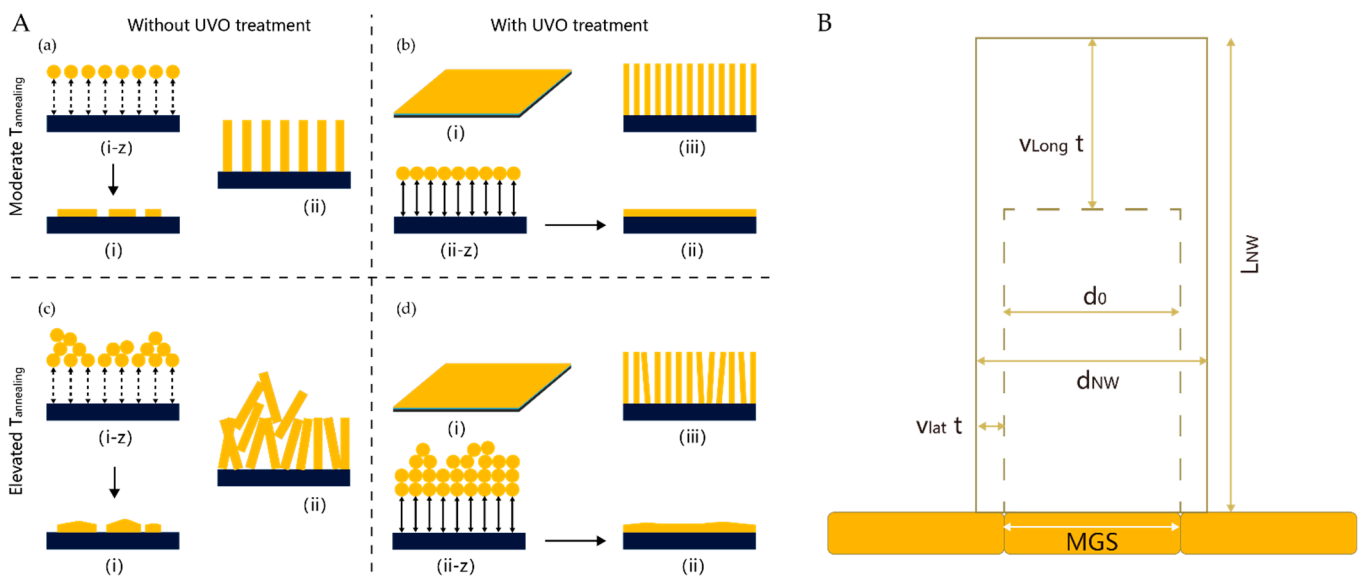


Figure 3. (A) Schematics of ZnO NW growth depending on substrate surface conditions and seed layer: (a) Without the ultraviolet ozone (UVO) treatment under a lower annealing temperature ($T_{annealing}$); (b) with UVO treatment; (c,d) with varied $T_{annealing}$ conditions [67]; (B) schematic representation of the NWs; growth [68].

Table 1. Factors influencing the morphology of hydrothermally grown NWs.

Conditions		Verticality	Density	Mean Length	Mean Diameter	Crystallinity
Seed layer properties	Thickness [67–69]	-	✓	-	✓	-
	Surface roughness [65,68,69]	✓	✓	-	✓	-
	Texture coefficient [66]	-	✓	-	-	-
	Mean grain size [66,70]	-	✓	✓	✓	-

Table 1. Cont.

Conditions	Verticality	Density	Mean Length	Mean Diameter	Crystallinity
Nucleation site density [69,71]	-	√	-	-	-
Crystal orientation [67,72]	√	-	-	-	√
Growth time [57,60,62,73]	-	-	√	√	√
Concentration of solution [57,60,62,74]	-	√	√	√	√
Temperatures [57,60,62,73,75]	√	-	√	√	√
pH [57,62,75–77]	-	√	√	√	-
Post-annealing treatment [77,78]	√	-	-	-	√

3. Effect of ZnO Nanowire Morphology on the SCs

3.1. Basic Physical Characteristics for IBHJ Photovoltaic Device

The current density in typical silicon p–n junction SCs is given by the sum of the drift currents in an electric field and the diffusion currents [79,80],

$$J = qE(n\mu_e + p\mu_h) + q\left(D_e \frac{dn}{dx} + D_h \frac{dp}{dx}\right) \quad (1)$$

where n and p are the electron and hole concentration, respectively, $\mu_{e(h)}$ is the majority carrier mobility, E is the electric field in the device, and D_e and D_h are the electron and hole diffusion coefficients. Generally, the CQD absorption layer is treated as a bulk semiconductor to describe phenomena such as drift and diffusion, carrier generation and recombination, and transport and trapping in CQD films [81]. In a depleted heterojunction CQDSC, a planar heterojunction is formed between the QD film and a wider bandgap electrode, which establishes a depletion region. The effective carrier extraction length is defined as $W_{QD} + L_D$, where W_{QD} is the width of the depletion region residing in the QD absorption layer and L_D is the minority carrier diffusion length [82]. The depletion region width is determined by the doping concentration of the material, which features a trade-off with the open circuit voltage (V_{OC}). QD materials with low defect density and high carrier mobility enable the efficient extraction of photogenerated carriers in the quasineutral region through the diffusion process. Photocarriers generated in regions further away from the depletion region than their L_D recombine before they can be extracted. This limited extraction length results in a compromise between the extraction of carriers and the absorption of light. IBHJ structures can break this balance by decoupling the directions of photon absorption and charge collection. A typical IBHJ structure is shown in Figure 4a, where a three-dimensional depletion heterojunction is formed between the NW and the QD absorber layer. Due to the optimized collection of optical carriers and improved light trapping effect, QDSCs employing this structure usually feature enhanced short-circuit current density (J_{SC}) than their planar counterparts. The PV performances of the QDSCs incorporating ZnO NWs are gathered in Table 2.

Table 2. PV performances of the QDSCs integrating ZnO NW arrays.

Photoanode	QD Material	IBHJ QDSC Structure	J _{SC} (mA cm ⁻²)	V _{OC} (mV)	FF	PCE (%)
ZnO NWs	PbSe [83]	ITO/ZnO/PbSe-EDT/ α -NPD/Au	18.6	420	0.25	1.97
	PbS [84]	ITO/ZnO/PbS-BDT/MoO ₃ /Au	17.9	600	0.40	4.3
	PbS [85]	FTO/ZnO/PbS-CTAB/Au	34.47	361	0.488	6.074
	PbS [86] ^a	FTO/ZnO/PbS-CTAB/Au	30.7	420	0.478	6.16
	PbS [87]	FTO/ZnO/PbS-CTAB/Au	27.9	422	-	6.03
	PbS [88]	FTO/ZnO/PbS-CTAB/Au	28.8	419	0.47	5.7
	PbS [89] ^b	FTO/ZnO/PbS-TBAI/PbS-EDT/Au	21.51	520	0.450	5.04
	PbS [36]	ITO/ZnO/PbS-TBAI/PbS-EDT/Au	29.4	570	0.57	9.6
	PbS [32] ^c	ITO/ZnO/PbS-TBAI/PbS-EDT/Au	17.81	490	0.435	3.81
	PbS [90]	FTO/ZnO/PbS-TBAI/Au	27.6	351	0.486	4.70
	PbS [91] ^d	FTO/ZnO/PbS-TBAI/PbS-EDT/Au	26.0	497	0.56	7.2
	PbS [92] ^e	FTO/ZnO/PbS-CTAB/Au	23.2	603	0.56	7.78
	PbS [35] ^f	ITO/ZnO/PbS-TBAI/PbS-EDT/Au	27.5	540	0.64	9.52
PbS [93] ^g	ITO/ZnO/PbS-TBAI/PbS-EDT/Au	31.1	610	0.57	10.8	

^{a,d} TiO₂-passivation. ^b Mg(OH)₂-passivation. ^c Flexible IBHJQDSC. ^e SnO₂-passivation. ^f ABA(4-aminobenzoic acid)-passivation. ^g H-plasma-passivation.

The depletion width of the CQD photovoltaic devices can be characterized by employing capacitance-voltage spectroscopy. The total depletion width (W_{DT}) of the device can be obtained as follows [94],

$$W_{DT} = \sqrt{\frac{qN_{QD}N_{ZnO}\epsilon_{QD}\epsilon_{ZnO}}{2(\epsilon_{QD}N_{QD} + \epsilon_{ZnO}N_{ZnO})}}(V_{bi} - V) \quad (2)$$

where N_i and ϵ_i ($i = QD, ZnO$) are the carrier density and permittivity of the n-type ZnO and p-type QDs, respectively. The value V_{bi} is the built-in potential and V is the applied bias. N_{ZnO} is usually the known parameter while, the carrier concentration of the CQD film is always obtained using Mott-Schottky analysis by fitting the linear region of $1/C^2$ (vicinity of V_{bi}). From W_{DT} , the corresponding depletion region into the CQD film can be obtained as

$$W_{QD} = W_{DT} \frac{\epsilon_{ZnO}N_{ZnO}}{\epsilon_{ZnO}N_{ZnO} + \epsilon_{QD}N_{QD}} \quad (3)$$

With the lifetime and mobility known (mobility can be calculated from the SCLC regime), the diffusion length can easily be calculated according to the formula,

$$L_D = \sqrt{\frac{k_B T}{e} \mu \tau} \quad (4)$$

where k_B is the Boltzmann constant, T is the temperature, e is the elementary charge, μ is the electron mobility, and τ is the carrier lifetime. Other measurement methods of L_D can be seen in the study of Zhitomirsky et al. [95].

3.2. Density of Nanowires

Generally speaking, the density of NW arrays is an important factor affecting the performance of IBHJ SCs. Although NW arrays with high density can speed up the extraction of photocarriers, this leads to a lower volume filling fraction of the QD light-absorbing materials. More importantly, NW arrays with high density feature larger interface areas, which undoubtedly increase the carrier recombination at the interface and, hence, a dramatic V_{OC} loss. In addition, studies have shown that appropriate density control can enhance the capture ability of incident light. Therefore, it is of great practical significance to analyze the density regulation mechanism of NW arrays in detail. Progress in this area has generally been slow for two reasons. On the one hand, accurate and high-quality synthesis methods, such as photolithography and vapor deposition, often require expensive equipment, which runs counter to the goal of the large-scale application of QD photovoltaic devices. On the other hand, NWs grown by simple hydrothermal synthesis methods usually feature higher area density and more surface defects, and their morphology control is usually more complex.

A typical IBHJ SC prepared using hydrothermal NW array is shown in Figure 8a. Due to the high density of the NWs, the QD materials between NWs are usually completely exhausted. In this case, the surface recombination of NWs and the light harvesting efficiency (LHE) are the main considerations. Theoretically, the lower the nanowire density, the less constrained the surface recombination, provided that carriers can be collected efficiently. The usefulness of surface defect passivation is a clear indirect proof of this point. Ozu et al. [92] used SnO_2 layers to passivate the surface of ZnO NWs, and the PCE of the NW CQDSCs was improved from 5.6 to 7.8% (Figure 4). They attributed this to the reduced deep-level defect density and an optimized band-gap arrangement. For effective light management in the IBHJ structures, too large or too small an area density leads to higher light reflectance, as shown in Figure 5a, and an appropriate area density eventually leads to higher light absorption and higher J_{SC} . Recently, Tavakoli Dastjerdi et al. [93] obtained a champion device with a PCE of 10.1% by tuning the areal density of ZnO NWs (≈ 150 per μm^2) by controlling the precursor concentration. In short, the density control of NWs requires a balance between the interface area and the light trapping effect of NWs. However, this is all based on satisfying the effective carrier collection, because spacing that is too large leads to poor carrier collection between NWs.

3.3. Length of Nanowires

The length of NWs is another important factor affecting device performance, and related studies have been widely reported. Studies have shown that both the total PCE and J_{SC} increase with the length of NWs under the condition of constant thickness of the QD absorption layer, as revealed in Figure 5b [83]. The PCE of the device increases with the thickness of the QD layer and eventually decreases due to bulk recombination and increasing series resistance under the condition that the length of NWs is constant as shown in Figure 5c [91]. In principle, long NW arrays allow the device to adopt a thicker QD absorption layer and can also enhance the light harvesting efficiency (LHE). However, increased device thickness eventually results in the deterioration of the carrier collection for a constant photocarrier diffusion length. Increasing the nanowire length causes poorer charge collection, since holes photoexcited near the front electrode must travel a long distance [88]. In addition, longer NWs mean a larger surface area, which leads to an increase in interfacial recombination events and, thus, a decreased V_{OC} .

Recently, Cheng et al. [91] fabricated devices with varied NW lengths to investigate the role of NWs in SCs. They found that the PCE reached its maximum under certain conditions and then gradually decreased, as shown in Figure 6. Through frequency domain time difference (FDTD) simulation, they found that internal light scattering and local light concentration caused by 3D structures may result in changes to carrier recombination dynamics. Increased internal scattering with longer NWs causes the light to concentrate in a certain region and, hence, an increased carrier recombination rate. Therefore, the

light trapping effect of NWs needs to be studied in detail to evaluate whether they are beneficial or harmful to a particular device. Notably, the QD absorber layer must slightly cover the NW arrays to avoid direct contact between the top ohmic contact and the ZnO. Jean et al. [84] found that the thermally evaporated MoO₃ interlayer, used to protect the QDs from damage during the destructive reverse contact deposition, could also act as a physical buffer layer to reduce the problem of short-circuit between the NWs and the back electrode.

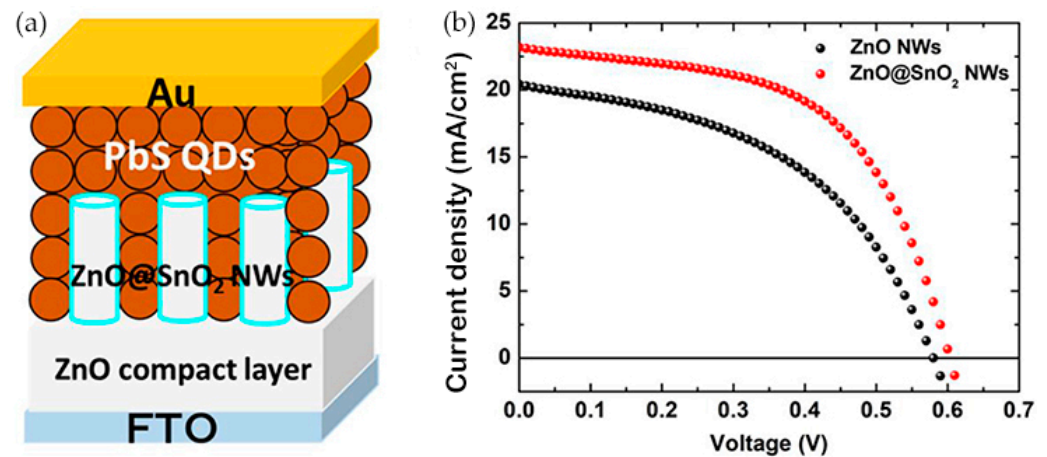


Figure 4. (a) Structural illustration of ZnO NW-based CQDSCs with SnO₂ passivation layers; (b) the J-V characteristics of ZnO NW CQDSCs with or without SnO₂ passivation [92].

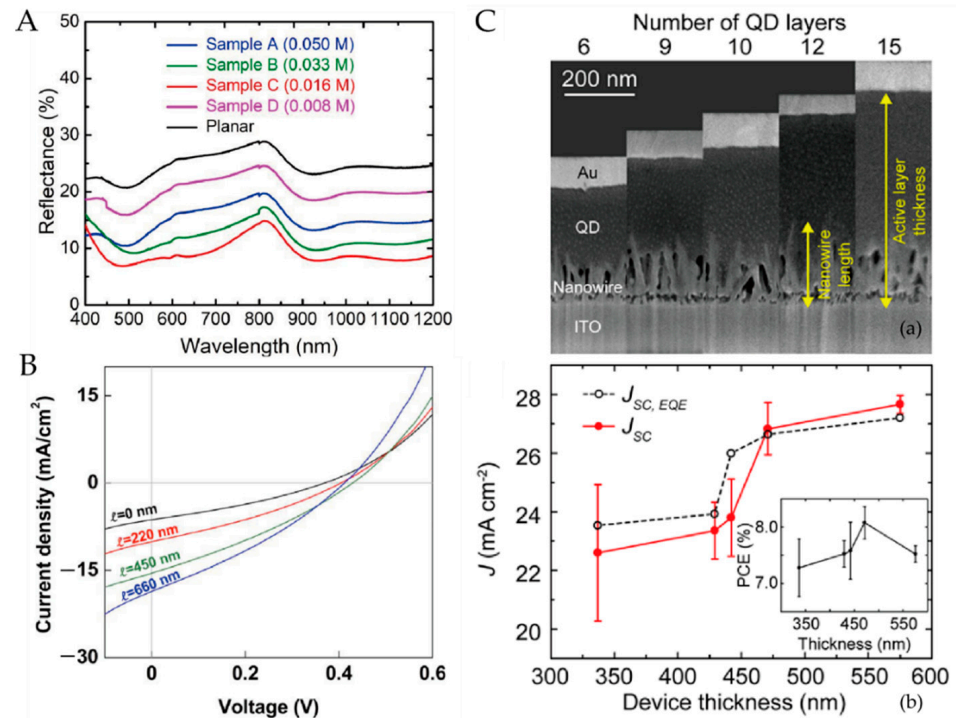


Figure 5. (A) Reflectance spectra of ZnO NWs with different areal densities grown on certain substrate [93]; (B) I-V curves of CQDSCs assembled with different length NWs [83]; (C) (a) SEM images of NW CQDSCs with different NW lengths, (b) corresponding device performance of different CQD layers [91].

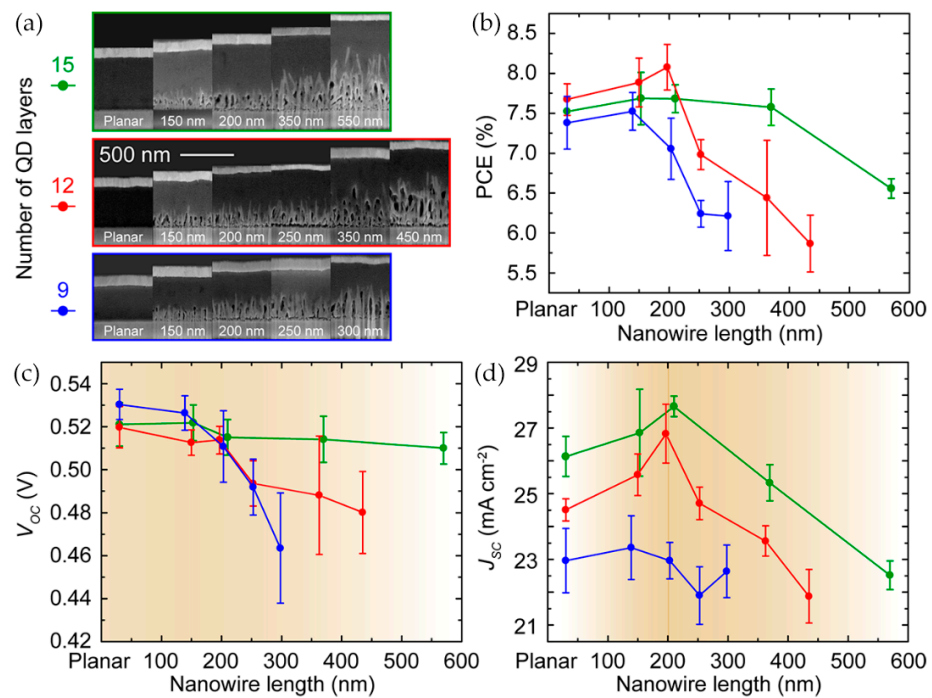


Figure 6. Performance variations of devices with different characteristics: (a) SEM images of devices with different NW lengths and CQD layers; (b) PCE, (c) V_{oc} , and (d) J_{sc} for sets of devices with different conditions [91].

4. Optimization Strategies of IBHJ QDSCs Based on ZnO NWs

4.1. Geometrical Morphology Optimization of Nanowires

The original intention to develop this bulk heterojunction structure was to increase the electrical contact area between the donor and the acceptor so that the photocarriers can be collected before they are captured by trap states. Moreover, NWs allow the light absorption and carrier extraction to be controlled independently [83]. Therefore, our core aim can be summarized as obtaining efficient carrier extraction and the increased thickness of light-absorbing materials. As early as 2012, Kramer et al. [96] proposed the spacing of nanopillars in their research on TiO₂ NWs QDSCs (Figure 7). However, longitudinal carrier collection is neglected, and this process often affects the overall thickness of the SCs.

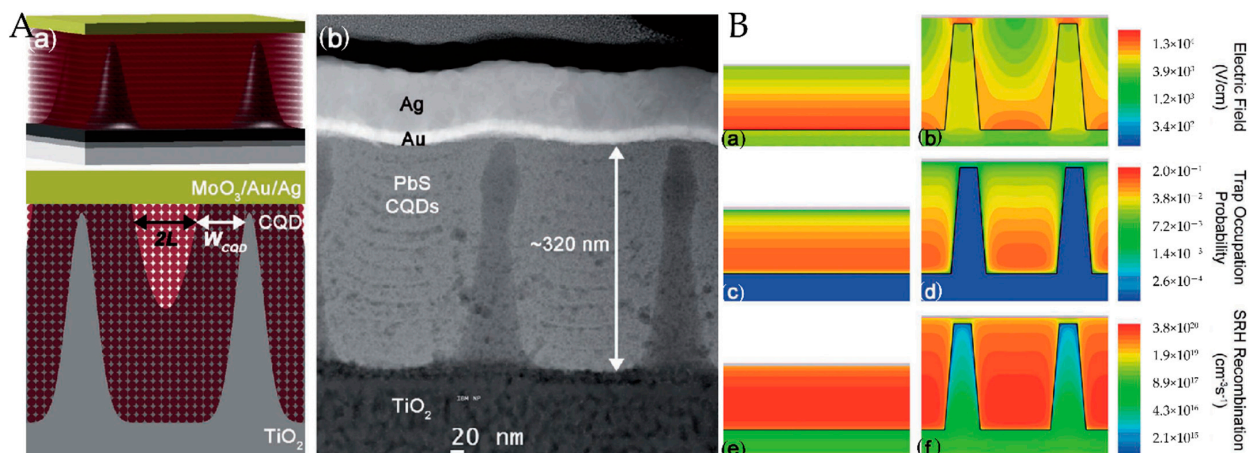


Figure 7. (A) (a) Schematic and (b) SEM images of CQDSCs; (B) electric field distributions, trap occupation, and SRH recombination of planar and nanopillar architectures [96].

Considering the efficient collection of photocarriers, it is necessary to distinguish between the electron and hole collection processes. To collect photogenerated electrons efficiently, the pitch size of the NWs should meet the following requirements (Figure 8),

$$d_{np-np} < 2 \times (W_{QD} + L_D) \quad (5)$$

$$d_{top} < W_{QD} + L_D \quad (6)$$

where d_{np-np} is the average spacing of NWs and d_{top} is the distance from the top of the NW to the back electrode. Notably, d_{top} is an upper bound on collection length. The depletion situation at the top of the nanowires is usually more complicated. Electrons are mainly collected horizontally, whereas holes often need to be transported vertically to the host electrode to form photocurrents. Therefore, the limited collection length of holes directly limits the length of the NWs and, thus, the thickness of the light-absorbing layer material,

$$D_{QD} < L + W_{QD} + L_D \quad (7)$$

where D_{QD} is the thickness of the QD absorption layer and L is the mean length of the NWs, which is limited to the hole collection length. Although studies have shown that holes in PbS QDs can diffuse a distance of over 1000 nm or longer under certain conditions [88], experimental and theoretical analysis is still needed to determine the optimal hole collection length. There are indications that even if IBHJ QDSCs with ultra-long NWs (1 μm to 2 μm) offer considerable efficiency, poor hole collection is likely to be the main factor limiting their efficiency. Experiments have shown that the external quantum efficiency decreases as the NWs grow in the short-wavelength regions, while the near-infrared band light increases as the NWs grow; this seems to be a good proof [91], since short-wavelength light is usually absorbed at the top of the cell and the holes usually feature a long collection distance. A QD absorption layer in the NW root area is likely to form a dead zone because holes are likely to quench or be captured in traps in the process of diffusion to the back electrode. Only near the NW top and the bottom of the SCs do the light absorption layer, NWs, and back electrode form an effective electrical pathway. A more detailed mechanism can be explored to a certain extent by using more sophisticated FDTD modeling to simulate the recombination of carriers in the QD region between the NWs. Furthermore, it is worth mentioning that the above parameters usually need to be determined according to the actual situation. For example, the width of the depletion region on the QD side usually depends on the doping concentration of the material. Here, we summarize some parameters of the bulk heterojunction formed between PbS quantum dots passivated by different ligands and ZnO in recent years (Table 3).

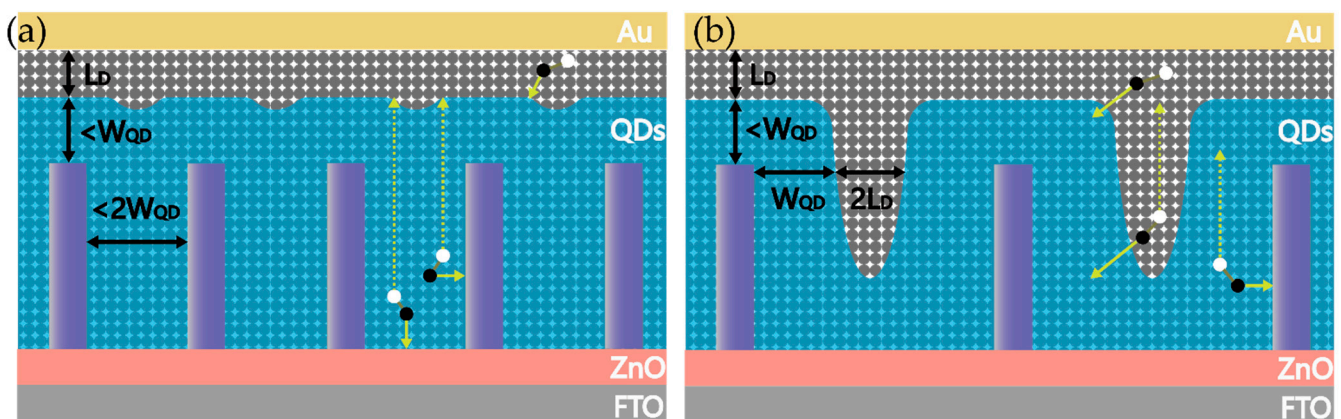


Figure 8. (a) IBHJ structure based on hydrothermal method; (b) ideal IBHJ structure.

Table 3. Characteristic parameters of several lead chalcogenide QD material layers.

Ligand	CQD Material	CQDSC Structure	Doping Density (cm ⁻³)	Depletion Width (nm)	Diffusion Lengths (nm)	PCE (%)
Organic ligand	PbS-MPA [95]	-	-	-	30	-
	PbS-MPA [97]	-	-	-	70	-
Halide ligand	PbS-PbX ₂ [98]	ITO/ZnO/PbS-PbX ₂ /PbS-EDT/Au	9.94 × 10 ¹⁶	165	52	7.2
	PbO-PbS-TBAI [99]	ITO/ZnO/PbS-TBAI/PbS-EDT/Au	-	-	61	9.4
	PbAc-PbS-TBAI [99]	ITO/ZnO/PbS-TBAI/PbS-EDT/Au	-	-	95	10.8
	PbS-TBAI [95]	-	-	-	70	-
	PbS-TBAI [94]	ITO/ZnO/PbS-TBAI/PbS-EDT/Au	7.3 × 10 ¹⁶	61.0 (at maximum PCE)	85	8.7
	PbS-I ₂ + TBAI [94]	ITO/ZnO/PbS-I ₂ + TBAI/PbS-EDT/Au	6.8 × 10 ¹⁶	62.5 (at maximum PCE)	115	10.1
	PbS-MPA + CdCl ₂ [100]	FTO/ZnO/PbS-MPA + CdCl ₂ /MoO _x /Au/Ag	1 × 10 ¹⁵ –1 × 10 ¹⁶	-	80	7.6
Hybrid ligand	PbS-PbX ₂ + MPE [98]	ITO/ZnO/PbS-PbX ₂ + MPE/PbS-EDT/Au	1.96 × 10 ¹⁶	288	94	9.6
	PbS-MPA/CdCl ₂ [97]	-	-	-	230	-

As the main geometric parameter, the diameter of the nanowires has rarely been mentioned. Generally, the diameter of the NWs should not be too small, despite their high doping relative to QD materials. To achieve the maximum depletion width in the radial direction of the NWs, the diameter of the nanowire must be at least twice the depletion width of the ZnO NW [29]. Moreover, NWs that are too thin are easy to break during assembly due to their poor mechanical properties. In order to satisfy these conditions, the light trapping effect should receive sufficient attention. A high LHE can be achieved by adjusting the density and length of the NWs. This process, however, is often associated with the surface area of the nanowires. Striking a balance between low surface area and optimized light capture is also a critical issue. The final consideration is the surface passivation of the NWs, which is discussed in the next section.

4.2. Passivation of Defects in Nanowires

ZnO NWs prepared using the low-temperature HT procedure usually feature more defect states, including shallow-level trapping states originating in the vacancies or interstitials of zinc [101]; and deep level trapping states, which are formed by oxygen vacancy, hydroxyl groups, and excess oxygen [102]. Studies have shown that shallow defect states in ZnO can not only improve the electron mobility of ZnO, but also act as an additional path for electron injection from the QD layer to the NWs in some cases [103]. Instead, the deep-level trapping states are the critical target of defect passivation because they mainly serve as the recombination centers of photocarriers [104]. Generally, green and

yellow emissions in the PL spectra of ZnO are assigned to deep-level defects (red emissions are associated with either surface oxygen or surface OH groups), while violet and blue emissions are related to shallow defects [101]. A relevant description is presented in the article by Vempati et al., as shown in Figure 9a. Hence, we can estimate the defect density of ZnO NWs from these emissions.

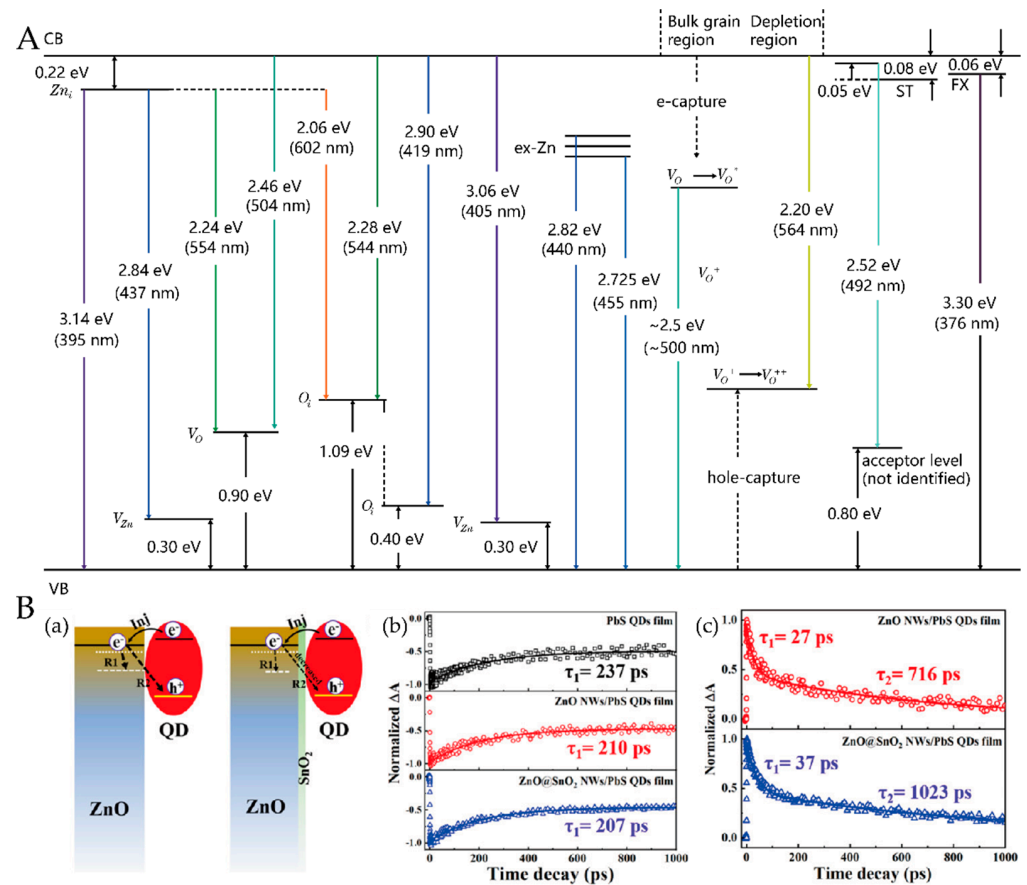


Figure 9. (A) Energy level diagram showing some of the principal defect levels in ZnO [101]; (B) (a) charge dynamic processes occurring at the ZnO NW/QD film interface. TA decay curves of the PbS QD film, ZnO NW/PbS QD film, and ZnO@SnO₂ NW/PbS QD film with a pump light of 470 nm and probe lights of (b) 960 and (c) 1500 nm [104].

The defect concentrations of HT-grown ZnO NWs can be significantly reduced by annealing [105]. Xu et al. [106] successfully eliminated or passivated the defect-related PL emissions of ZnO NWs by employing sealed post-annealing treatment. Concerning again the surface defects of NWs, Kim et al. [107] successfully reduced the number of excess-oxygen-related defects through thermal annealing in an H₂ ambient atmosphere above 300 °C. The excess-oxygen-related deep-level emissions were quenched completely, while the near band-edge emissions were greatly enhanced when H atoms were incorporated into ZnO NWs. These H atoms are most likely to exist in the form of shallow donors and may be removed after annealing at 400 °C [108–110]. Concerning the desorption of hydroxyl groups, Shi et al. [108] confirmed that annealing at 150 °C results in the removal of OH groups, but it may also introduce other hydrogen-related impurities. In a study of the overall performance of devices, Chang et al. [86] found that 350 °C might be the optimal annealing temperature, and the lowest defect emission and sufficient ZnO crystallinity were obtained at this temperature.

More recently, Tavakoli Dastjerdi et al. [93] passivated ZnO NW surface states using the hydrogen plasma treatment. Compared with the untreated NWs, the PL spectrum of the H-plasma-treated ZnO NWs showed a clear enhancement of near-band emissions and

a remarkable quenching of the visible emission peak. Through X-ray electron spectroscopy (XPS) analysis, the authors found an increase in the number of hydroxyl groups and attributed this to the passivated O-dangling bonds. Despite the increase in hydroxyl groups, reduced surface oxygen defects and possible H doping may lead to an improved overall performance [93,107]. Shi et al. [35] obtained a 9.3% PCE by introducing ABA-modified ZnO NW arrays in QDSCs. In addition to the passivation of ZnO surface defect states, ABA modification can change the interfacial dipole momentum between ZnO NWs and CQDs, thus effectively increasing the vacuum level.

Parallel to the class of passivation strategies for post-annealing and surface treatment, depositing organic/inorganic coatings to passivate the surface of ZnO NWs were also investigated [91,109]. Zhang et al. [104] clarified in detail the influence of surface SnO₂ passivation on the charge dynamic process in ZnO NWs by employing time-resolved photoluminescence (TRPL) and transient absorption (TA) spectroscopy techniques, as shown in Figure 9b. After SnO₂ passivation, the PL intensity of the deep-level defects related emission clearly decreased and the time constants of the two recombination pathways (R1 pathway, in which free electrons are trapped by defect states, and the R2 pathway, in which free electrons are recombined with the holes of PbS QDs) increased, which confirmed the positive effect of the surface passivation layer. Interestingly, Zang et al. [89] revealed the possibility of insulating interfacial modification with a Mg(OH)₂ interlayer; the performance of the IBHJ QDSCs improved, with a V_{OC} and PCE of 520 mV and 5.04%, respectively. Through the chemical reaction between ZnO and the TiO₂ precursor, Chang et al. [86] fabricated TiO₂-passivated ZnO NW CQDSCs. They provided direct proof of the reduced recombination in the surface-passivated cell by transient open-circuit photovoltage decay measurements. The results showed that the TiO₂-passivated cells exhibited much slower decay processes than those of the bare unpassivated cells. More recently, Cheng et al. [91] significantly minimized V_{OC} losses by passivating a ZnO nanowire surface with ALD TiO₂. Compared with unpassivated devices, the surface-passivated NW devices featured higher J_{sc} and V_{OC}, which was attributed to the passivated surface defects. The performance comparison before and after the passivation process can be seen intuitively in Table 4.

Table 4. Performance optimization of IBHJ QDSCs with passivation strategies.

Passivation Strategy	CQDSC Structure	-	J _{sc} (mA/cm ²)	V _{oc} (mV)	FF	PCE (%)
H-plasma-passivation [93]	ITO/ZnO NWs/PbS-TBAI/PbS-EDT/Au	non-treated	30.0	591	0.56	9.9
		H-plasma treated	31.1	610	0.57	10.8
ABA-passivation [35]	ITO/ZnO NWs/PbS-TBAI/PbS-EDT/Au	non-treated	27.4	510	0.60	8.41
		ABA-treated	27.5	540	0.64	9.52
Mg(OH) ₂ [89]	FTO/ZnO NWs/PbS-TBAI/PbS-EDT/Au	without Mg(OH) ₂	22.62	390	45.66	4.03
		with Mg(OH) ₂	21.51	520	45.08	5.04
SnO ₂ [92]	FTO/ZnO NWs/PbS-CTAB/Au	without SnO ₂	20.4	580	0.47	5.55
		with SnO ₂	23.2	603	0.56	7.78
CBD-TiO ₂ [86]	FTO/ZnO NWs/PbS-CTAB/Au	without TiO ₂	28.7	279	0.430	3.50
		with TiO ₂	30.7	420	0.478	6.16
ALD-TiO ₂ [91]	FTO/ZnO NWs/PbS-TBAI/PbS-EDT/Au	without TiO ₂	25.3	505	0.54	6.9
		with TiO ₂	26.0	497	0.56	7.2

4.3. Other Optimization Strategies

The effective infiltration of QDs in NW arrays is an important means of reducing interfacial defects. However, an important fact is that IBHJ QDSCs may feature a large number of voids, and these voids could cause a sharp decline in the performance of devices. Recently, more and more evidence has shown that the deposition method exerts an important effect on the morphology of thin films. Although the traditional spin-coating deposition method features advantages in small-scale fabrication due to its simplicity and practicability, it may be difficult to control the morphology due to the uneven shear stress distribution during the coating process [86]. In addition, it is still debatable whether mechanical fractures occur in the process of high-speed rotation of NW arrays, which aggravate the deterioration of the performance. A new deposition method based on the meniscus was proposed. “Meniscus-guided” means that the meniscus is shifted across the substrate by a coating head or viscous force to effectively guide and control film deposition [110]. Due to the inherent directivity of the coating process, the QDs can be effectively deposited by penetration. This method is appropriate for large-scale use. By simultaneously controlling the growth orientation of the NWs and introducing convective assembly as the CQD deposition technique, the dense packing and efficient infiltration of CQDs can be effectively improved. In this way, Shi et al. produced a finely interpenetrating OBHJ structure between ZnO NW arrays and PbS CQDs, and demonstrated a PCE of 9.92% in the devices [35].

QDSC design for stability is also an important subject for PV commercialization. Without considering the NW light aggregation effect and similar structural issues, IBHJ QDSCs are similar to planar QDSCs in that their device lifetime is mainly dependent on the QD material itself. Current synthesis and defect passivation techniques have been effective in reducing the oxidation sites associated with the stability of materials. PbS QDSCs can maintain their initial PCE in air with no encapsulation for 30 days [108]. In another study, ZnO NW-based CQDSCs exhibited excellent stable properties (the PCE was almost constant) after being stored in air for 250 days [92]. Further stability optimization strategies need to consider the mechanism of ambient factors (such as oxygen, water, and increased temperatures or high intensities of illumination) affecting the QDs. The intrinsic properties of the QDs themselves and their interplay with other materials are also factors to be considered [110].

5. Conclusions

IBHJ QDSCs form a 3D depletion region for the high-efficiency utilization of solar energy, which allows the incorporation of more QD material while maintaining efficient charge collection. As ETLs, ZnO NW structures should offer optimal electric continuity and need to be relatively transparent to visible light to avoid photon loss. In this study, an assessment was performed on the previous research into the preparation of ZnO NWs, and the effect of the ZnO NW morphology on performance and the optimization strategies of IBHJ QDSCs were summarized. The conclusions and outlooks are as follows:

- (1) The HT method is more suitable for the large-scale application of IBHJ QDSCs due to its advantages of low temperature, high yield, and easy processing. The morphology of HT-grown NWs is influenced by the seed layer properties, growth time, concentration, temperatures, PH, and post-treatment conditions. However, it is necessary to investigate the mechanism of these influencing factors for the preparation of NWs with controllable morphologies. Furthermore, the optimization of surface defects and internal defects and the reliability of HT-doping elements also need to be studied further to improve the performance of the ETL and to tune the band-gap arrangement.
- (2) The density of the NW affects the filling volume of QD materials. High-density NW arrays not only feature a large V_{OC} loss due to their large interface area, but also cause high reflectivity in the SCs, reducing the light absorption. The length of the nanowires determines the depth of the carrier collection and further affects the thickness of the SCs. However, long NWs often result in poor hole collection and increase the interface

area. In addition, the length of the nanowires affects the light trapping effect of the 3D structure, and may cause the aggregation of light absorption and ultimately affect the recombination of the carriers.

- (3) The geometric morphology of the NW exerts a great influence on the transmission and collection of photocarriers. The optimization of NW spacing needs to take account of the transverse collection of electrons, while the length of the NW and the thickness of the SC absorption layer need to be determined after comprehensively analyzing the longitudinal aggregation of holes. In order to satisfy the carrier collection conditions as far as possible, reducing the NW density can increase the filling volume of QD light absorption material.
- (4) In order to further optimize the 3D structure, more accurate carrier transport mechanism analysis needs to be carried out in combination with electrical simulation to determine the optimal electrical structure. The light-trapping effect caused by NWs also needs to be more accurately analyzed, since poor light scattering may lead to local light aggregation and thus affect the distribution and collection efficiency of photocarriers.
- (5) The passivation of the NW surface is an important way to improve the V_{OC} of IBHJ QDSCs. Passivation strategies commonly include post-annealing, H-plasma treatment, and ABA surface treatment. Moreover, the addition of $Mg(OH)_2$, SnO_2 , and TiO_2 buffer layers on the surface of NWs also effectively improves the performance of SCs. However, the effects of the passivation layer (including the passivation mechanism of the defects and the band arrangement of the battery) on the three-dimensional heterojunction remain to be explored. A comparative study of different passivation layers may be helpful in this regard.

Author Contributions: M.X. and R.W. designed and engineered the structure of the paper; M.X. helped analyze the cited papers; L.W. wrote the paper with support from M.X. and R.W. All authors have read and agreed to the published version of the manuscript.

Funding: This research was funded by National Natural Science Foundation of China (NSFC), grant number [No. 51906013] and the Pyramid Talent Training Project of Beijing University of Civil Engineering and Architecture, grant number [JDYC20200316].

Institutional Review Board Statement: Not applicable.

Conflicts of Interest: The authors declare no conflict of interest.

References

1. Gil, L.; Bernardo, J. An Approach to Energy and Climate Issues Aiming at Carbon Neutrality. *Renew. Energy Focus* **2020**, *33*, 37–42. [[CrossRef](#)]
2. Khalid, S.; Sultan, M.; Ahmed, E.; Ahmed, W. Chapter 1-Third-Generation Solar Cells. In *Emerging Nanotechnologies for Renewable Energy*; Ahmed, W., Booth, M., Nourafkan, E., Eds.; Micro and Nano Technologies; Elsevier: Amsterdam, The Netherlands, 2021. [[CrossRef](#)]
3. Green, M.; Emery, K.; Hishikawa, Y.; Warta, W.; Dunlop, E.; Barkhouse, D.; Gunawan, O.; Gokmen, T.; Todorov, T.; Mitzi, D. Solar cell efficiency tables (version 40). *IEEE Trans. Fuzzy Syst.* **2012**, *20*, 1114–1129. [[CrossRef](#)]
4. Weller, H. Colloidal Semiconductor Q-Particles: Chemistry in the Transition Region Between Solid State and Molecules. *Angew. Chemie Int. Ed. English* **1993**, *32*, 41–53. [[CrossRef](#)]
5. Schaller, R.D.; Klimov, V.I. High Efficiency Carrier Multiplication in PbSe Nanocrystals: Implications for Solar Energy Conversion. *Phys. Rev. Lett.* **2004**, *92*, 1–4. [[CrossRef](#)]
6. Goodwin, H.; Jellicoe, T.C.; Davis, N.J.L.K.; Böhm, M.L. Multiple Exciton Generation in Quantum Dot-Based Solar Cells. *Nanophotonics* **2018**, *7*, 111–126. [[CrossRef](#)]
7. Knig, D.; Casalenuovo, K.; Takeda, Y.; Conibeer, G.; Guillemoles, J.F.; Patterson, R.; Huang, L.M.; Green, M.A. Hot Carrier Solar Cells: Principles, Materials and Design. *Phys. E Low-Dimensional Syst. Nanostruct.* **2010**, *42*, 2862–2866. [[CrossRef](#)]
8. Marti, A.; Cuadra, L.; Luque, A. Quantum Dot Intermediate Band Solar Cell. *Conf. Rec. IEEE Photovolt. Spec. Conf.* **2000**, *2000*, 940–943. [[CrossRef](#)]
9. Luque, A.; Martí, A. The Intermediate Band Solar Cell: Progress toward the Realization of an Attractive Concept. *Adv. Mater.* **2010**, *22*, 160–174. [[CrossRef](#)] [[PubMed](#)]

10. Asahi, S.; Kaizu, T.; Kita, T. Adiabatic Two-Step Photoexcitation Effects in Intermediate-Band Solar Cells with Quantum Dot-in-Well Structure. *Sci. Rep.* **2019**, *9*, 1–8. [[CrossRef](#)]
11. McMeekin, D.P.; Mahesh, S.; Noel, N.K.; Klug, M.T.; Lim, J.C.; Warby, J.H.; Ball, J.M.; Herz, L.M.; Johnston, M.B.; Snaith, H.J. Solution-Processed All-Perovskite Multi-Junction Solar Cells. *Joule* **2019**, *3*, 387–401. [[CrossRef](#)]
12. Ikeri, H.I.; Onyia, A.I.; Vwawware, O.J. The Dependence of Confinement Energy on the Size of Quantum Dots. *Int. J. Sci. Res. Phys. Appl. Sci.* **2019**, *7*, 27–30. [[CrossRef](#)]
13. Shockley, W.; Queisser, H.J. Detailed Balance Limit of Efficiency of P-n Junction Solar Cells. *J. Appl. Phys.* **1961**, *32*, 510–519. [[CrossRef](#)]
14. Johnston, K.W.; Pattantyus-Abraham, A.G.; Clifford, J.P.; Myrskog, S.H.; MacNeil, D.D.; Levina, L.; Sargent, E.H. Schottky-Quantum Dot Photovoltaics for Efficient Infrared Power Conversion. *Appl. Phys. Lett.* **2008**, *92*, 1–4. [[CrossRef](#)]
15. Piliago, C.; Protesescu, L.; Bisri, S.Z.; Kovalenko, M.V.; Loi, M.A. 5.2% Efficient PbS Nanocrystal Schottky Solar Cells. *Energy Environ. Sci.* **2013**, *6*, 3054–3059. [[CrossRef](#)]
16. Zhang, Y.; Ding, C.; Wu, G.; Nakazawa, N.; Chang, J.; Ogomi, Y.; Toyoda, T.; Hayase, S.; Katayama, K.; Shen, Q. Air Stable PbSe Colloidal Quantum Dot Heterojunction Solar Cells: Ligand-Dependent Exciton Dissociation, Recombination, Photovoltaic Property, and Stability. *J. Phys. Chem. C* **2016**, *120*, 28509–28518. [[CrossRef](#)]
17. Spencer, B.F.; Leontiadou, M.A.; Clark, P.C.J.; Williamson, A.I.; Silly, M.G.; Sirotti, F.; Fairclough, S.M.; Tsang, S.C.E.; Neo, D.C.J.; Assender, H.E.; et al. Charge Dynamics at Heterojunctions for PbS/ZnO Colloidal Quantum Dot Solar Cells Probed with Time-Resolved Surface Photovoltage Spectroscopy. *Appl. Phys. Lett.* **2016**, *108*. [[CrossRef](#)]
18. Pattantyus-Abraham, A.G.; Kramer, I.J.; Barkhouse, A.R.; Wang, X.; Konstantatos, G.; Debnath, R.; Levina, L.; Raabe, I.; Nazeeruddin, M.K.; Gratzel, M. Depleted-Heterojunction Colloidal Quantum Dot Solar Cells. *ACS Nano* **2010**, *4*, 3374–3380. [[CrossRef](#)] [[PubMed](#)]
19. Rath, A.K.; Bernechea, M.; Martinez, L.; Pelayo Garcia De Arquer, F.; Osmond, J.; Konstantatos, G. Solution-Processed Inorganic Bulk Nano-Heterojunctions and Their Application to Solar Cells. *Nat. Photonics* **2012**, *6*, 529–534. [[CrossRef](#)]
20. Tang, J.; Liu, H.; Zhitomirsky, D.; Hoogland, S.; Wang, X.; Furukawa, M.; Levina, L.; Sargent, E.H. Quantum Junction Solar Cells. *Nano Lett.* **2012**, *12*, 4889–4894. [[CrossRef](#)] [[PubMed](#)]
21. Jia, Y.; Wang, H.; Wang, Y.; Shibayama, N.; Kubo, T.; Liu, Y.; Zhang, X.; Segawa, H. High-Performance Electron-Transport-Layer-Free Quantum Junction Solar Cells with Improved Efficiency Exceeding 10%. *ACS Energy Lett.* **2021**, 493–500. [[CrossRef](#)]
22. Chang, C.H.; Lee, Y.L. Chemical Bath Deposition of CdS Quantum Dots onto Mesoscopic TiO₂ Films for Application in Quantum-Dot-Sensitized Solar Cells. *Appl. Phys. Lett.* **2007**, *91*, 2–5. [[CrossRef](#)]
23. Kamat, P.V.; Bang, J.H. Quantum Dot Sensitized Solar Cells: Tale of Two Semiconductor Nanocrystals—CdSe and CdTe. *ACS Natl. Meet. B. Abstr.* **2009**, *3*, 1467–1476.
24. Sahu, A.; Garg, A.; Dixit, A. A Review on Quantum Dot Sensitized Solar Cells: Past, Present and Future towards Carrier Multiplication with a Possibility for Higher Efficiency. *Sol. Energy* **2020**, *203*, 210–239. [[CrossRef](#)]
25. Choi, M.J.; García de Arquer, F.P.; Proppe, A.H.; Seifitokaldani, A.; Choi, J.; Kim, J.; Baek, S.W.; Liu, M.; Sun, B.; Biondi, M.; et al. Cascade Surface Modification of Colloidal Quantum Dot Inks Enables Efficient Bulk Homo Junction Photovoltaics. *Nat. Commun.* **2020**, *11*, 1–9. [[CrossRef](#)]
26. Beard, M.C.; Luther, J.M.; Semonin, O.E.; Nozik, A.J. Third Generation Photovoltaics Based on Multiple Exciton Generation in Quantum Confined Semiconductors. *Acc. Chem. Res.* **2013**, *46*, 1252–1260. [[CrossRef](#)]
27. Johnston, K.W.; Pattantyus-Abraham, A.G.; Clifford, J.P.; Myrskog, S.H.; Hoogland, S.; Shukla, H.; Klem, E.J.D.; Levina, L.; Sargent, E.H. Efficient Schottky-Quantum-Dot Photovoltaics: The Roles of Depletion, Drift, and Diffusion. *Appl. Phys. Lett.* **2008**, *92*, 1–4. [[CrossRef](#)]
28. Fan, Z.; Razavi, H.; Do, J.W.; Moriwaki, A.; Ergen, O.; Chueh, Y.L.; Leu, P.W.; Ho, J.C.; Takahashi, T.; Reichertz, L.A.; et al. Three-Dimensional Nanopillar-Array Photovoltaics on Low-Cost and Flexible Substrates. *Nat. Mater.* **2009**, *8*, 648–653. [[CrossRef](#)]
29. Kayes, B.M.; Atwater, H.A.; Lewis, N.S. Comparison of the Device Physics Principles of Planar and Radial P-n Junction Nanorod Solar Cells. *J. Appl. Phys.* **2005**, *97*, 114302. [[CrossRef](#)]
30. Garnett, E.; Yang, P. Light Trapping in Silicon Nanowire Solar Cells. *Nano Lett.* **2010**, *10*, 1082–1087. [[CrossRef](#)]
31. Krogstrup, P.; Jørgensen, H.I.; Heiss, M.; Demichel, O.; Holm, J.V.; Aagesen, M.; Nygard, J.; Fontcuberta i Morral, A. Single-Nanowire Solar Cells beyond the Shockley-Queisser Limit. *Nat. Photonics* **2013**, *7*, 306–310. [[CrossRef](#)]
32. Wang, Y.; Su, W.; Zang, S.; Li, M.; Zhang, X.; Liu, Y. Bending-Durable Colloidal Quantum Dot Solar Cell Using a ZnO Nanowire Array as a Three-Dimensional Electron Transport Layer. *Appl. Phys. Lett.* **2017**, *110*, 1–6. [[CrossRef](#)]
33. Tavakoli Dastjerdi, H.; Prochowic, D.; Yadav, P.; Tavakoli, M.M. Luminescence Down-Shifting Enables UV-Stable and Efficient ZnO Nanowire-Based PbS Quantum Dot Solar Cells with JSC Exceeding 33 MA Cm⁻². *Sustain. Energy Fuels* **2019**, *3*, 3128–3134. [[CrossRef](#)]
34. Zhu, R.; Yang, R. Growth of Uniform Nanowires with Orientation Control. In *Synthesis and Characterization of Piezotronic Materials for Application in Strain/Stress Sensing*; Mechanical Engineering Series; Springer: Cham, Switzerland, 2018. [[CrossRef](#)]
35. Shi, G.; Kaewprajak, A.; Ling, X.; Hayakawa, A.; Zhou, S.; Song, B.; Kang, Y.W.; Hayashi, T.; Altun, M.E.; Nakaya, M.; et al. Finely Interpenetrating Bulk Heterojunction Structure for Lead Sulfide Colloidal Quantum Dot Solar Cells by Convective Assembly. *ACS Energy Lett.* **2019**, *4*, 960–967. [[CrossRef](#)]

36. Rekemeyer, P.H.; Chang, S.; Chuang, C.-H.M.; Hwang, G.W.; Bawendi, M.G.; Gradečak, S. Enhanced Photocurrent in PbS Quantum Dot Photovoltaics via ZnO Nanowires and Band Alignment Engineering. *Adv. Energy Mater.* **2016**, *6*, 1600848–1600854. [[CrossRef](#)]
37. Djurić, A.B.; Ng, A.M.C.; Chen, X.Y. ZnO Nanostructures for Optoelectronics: Material Properties and Device Applications. *Prog. Quantum Electron.* **2010**, *34*, 191–259. [[CrossRef](#)]
38. Gomez, J.L.; Tigli, O. Zinc Oxide Nanostructures: From Growth to Application. *J. Mater. Sci.* **2013**, *48*, 612–624. [[CrossRef](#)]
39. Baruah, S.; Dutta, J. Hydrothermal Growth of ZnO Nanostructures. *Sci. Technol. Adv. Mater.* **2009**, *10*. [[CrossRef](#)] [[PubMed](#)]
40. Susner, M.A.; Carnevale, S.D.; Kent, T.F.; Gerber, L.M.; Phillips, P.J.; Sumption, M.D.; Myers, R.C. Catalyst-Free ZnO Nanowires on Silicon by Pulsed Laser Deposition with Tunable Density and Aspect Ratio. *Phys. E Low-Dimensional Syst. Nanostruct.* **2014**, *62*, 95–103. [[CrossRef](#)]
41. Kaps, S.; Bhowmick, S.; Gröttrup, J.; Hrkac, V.; Stauffer, D.; Guo, H.; Warren, O.L.; Adam, J.; Kienle, L.; Minor, A.M.; et al. Piezoresistive Response of Quasi-One-Dimensional ZnO Nanowires Using an in Situ Electromechanical Device. *ACS Omega* **2017**, *2*, 2985–2993. [[CrossRef](#)] [[PubMed](#)]
42. Zheng, Z.; Gan, L.; Zhang, J.B.; Zhuge, F.; Zhai, T.Y. An Enhanced UV-Vis-NIR and Flexible Photodetector Based on Electrospun ZnO Nanowire Array/PbS Quantum Dots Film Heterostructure. *Adv. Sci.* **2017**, *4*, 1–8. [[CrossRef](#)]
43. Isakov, I.; Panfilova, M.; Sourribes, M.J.L.; Warburton, P.A. Growth of ZnO and ZnMgO Nanowires by Au-Catalysed Molecular-Beam Epitaxy. *Phys. Status Solidi Curr. Top. Solid State Phys.* **2013**, *10*, 1308–1313. [[CrossRef](#)]
44. Bi, N.; Zhang, L.; Zheng, Q.; Zhuge, F.; Li, J.; Gao, X.P.A.; Du, J. Control of ZnO Nanowire Growth and Optical Properties in a Vapor Deposition Process. *J. Mater. Sci. Technol.* **2017**, *33*, 850–855. [[CrossRef](#)]
45. Bhutto, W.A.; Soomro, A.M.; Nizamani, A.H.; Saleem, H.; Khaskheli, M.A.; Sahito, A.G.; Das, R.; Khan, U.A.; Saleem, S. Controlled Growth of Zinc Oxide Nanowire Arrays by Chemical Vapor Deposition (CVD) Method. *Int. J. Comput. Sci. Netw. Secur.* **2019**, *19*, 135–141.
46. Greene, L.E.; Law, M.; Tan, D.H.; Montano, M.; Goldberger, J.; Somorjai, G.; Yang, P. General Route to Vertical ZnO Nanowire Arrays Using Textured ZnO Seeds. *Nano Lett.* **2005**, *5*, 1231–1236. [[CrossRef](#)] [[PubMed](#)]
47. Li, C.; Fang, G.; Li, J.; Ai, L.; Dong, B.; Zhao, X. Effect of Seed Layer on Structural Properties of ZnO Nanorod Arrays Grown by Vapor-Phase Transport. *J. Phys. Chem. C* **2008**, *112*, 990–995. [[CrossRef](#)]
48. Serrano, A.; Arana, A.; Galdámez, A.; Dutt, A.; Monroy, B.M.; Güell, F.; Santana, G. Effect of the Seed Layer on the Growth and Orientation of the ZnO Nanowires: Consequence on Structural and Optical Properties. *Vacuum* **2017**, *146*, 509–516. [[CrossRef](#)]
49. Yang, P.; Yan, H.; Mao, S.; Russo, R.; Johnson, J.; Saykally, R.; Morris, N.; Pham, J.; He, R.; Choi, H.J. Controlled Growth of ZnO Nanowires and Their Optical Properties. *Adv. Funct. Mater.* **2002**, *12*, 323–331. [[CrossRef](#)]
50. Shin, H.S.; Sohn, J.I.; Kim, D.C.; Huck, W.T.S.; Welland, M.E.; Choi, H.C.; Kang, D.J. Density Control of ZnO Nanowires Grown Using Au-PMMA Nanoparticles and Their Growth Behavior. *Nanotechnology* **2009**, *20*, 085601. [[CrossRef](#)] [[PubMed](#)]
51. Si, H.; Kang, Z.; Liao, Q.; Zhang, Z.; Zhang, X.; Wang, L.; Zhang, Y. Design and Tailoring of Patterned ZnO Nanostructures for Energy Conversion Applications. *Sci. China Mater.* **2017**, *60*, 793–810. [[CrossRef](#)]
52. Chong, T.C.; Hong, M.H.; Shi, L.P. Laser Precision Engineering: From Microfabrication to Nanoprocessing. *Laser Photonics Rev.* **2010**, *4*, 123–143. [[CrossRef](#)]
53. Wei, Y.; Wu, W.; Guo, R.; Yuan, D.; Das, S.; Wang, Z.L. Wafer-Scale High-Throughput Ordered Growth of Vertically Aligned ZnO Nanowire Arrays. *Nano Lett.* **2010**, *10*, 3414–3419. [[CrossRef](#)]
54. Hu, H.; Huang, X.; Deng, C.; Chen, X.; Qian, Y. Hydrothermal Synthesis of ZnO Nanowires and Nanobelts on a Large Scale. *Mater. Chem. Phys.* **2007**, *106*, 58–62. [[CrossRef](#)]
55. Podrezova, L.V.; Porro, S.; Cauda, V.; Fontana, M.; Cicero, G. Comparison between ZnO Nanowires Grown by Chemical Vapor Deposition and Hydrothermal Synthesis. *Appl. Phys. A Mater. Sci. Process.* **2013**, *113*, 623–632. [[CrossRef](#)]
56. Chevalier-César, C.; Capochichi-Gnambodoe, M.; Leprince-Wang, Y. Growth Mechanism Studies of ZnO Nanowire Arrays via Hydrothermal Method. *Appl. Phys. A Mater. Sci. Process.* **2014**, *115*, 953–960. [[CrossRef](#)]
57. Amin, G.; Asif, M.H.; Zainelabdin, A.; Zaman, S.; Nur, O.; Willander, M. Influence of PH, Precursor Concentration, Growth Time, and Temperature on the Morphology of ZnO Nanostructures Grown by the Hydrothermal Method. *J. Nanomater.* **2011**, *2011*. [[CrossRef](#)]
58. Akgun, M.C.; Kalay, Y.E.; Unalan, H.E. Hydrothermal Zinc Oxide Nanowire Growth Using Zinc Acetate Dihydrate Salt. *J. Mater. Res.* **2012**, *27*, 1445–1451. [[CrossRef](#)]
59. Yang, W.; Wang, Y.; Zhen, Q.; Shi, W. Effect of Growth Time on Morphology and Photovoltaic Properties of ZnO Nanowire Array Films. *Rare Met.* **2011**, *30*, 676–680. [[CrossRef](#)]
60. Muchuweni, E.; Sathiaraj, T.S.; Nyakoty, H. Hydrothermal Synthesis of ZnO Nanowires on Rf Sputtered Ga and Al Co-Doped ZnO Thin Films for Solar Cell Application. *J. Alloys Compd.* **2017**, *721*, 45–54. [[CrossRef](#)]
61. Yu, J.; Yuan, Z.; Han, S.; Ma, Z. Size-Selected Growth of Transparent Well-Aligned ZnO Nanowire Arrays. *Nanoscale Res. Lett.* **2012**, *7*, 1–6. [[CrossRef](#)]
62. Gerbreder, V.; Krasovska, M.; Sledevskis, E.; Gerbreder, A.; Mihailova, I.; Tamanis, E.; Ogurcovs, A. Hydrothermal Synthesis of ZnO Nanostructures with Controllable Morphology Change. *CrystEngComm* **2020**, *22*, 1346–1358. [[CrossRef](#)]
63. Cao, B.; Cai, W. From ZnO Nanorods to Nanoplates: Chemical Bath Deposition Growth and Surface-Related Emissions. *J. Phys. Chem. C* **2008**, *112*, 680–685. [[CrossRef](#)]

64. Rakhsha, A.H.; Abdizadeh, H.; Pourshaban, E.; Golobostanfard, M.R.; Mastelaro, V.R.; Montazerian, M. Ag and Cu Doped ZnO Nanowires: A PH-Controlled Synthesis via Chemical Bath Deposition. *Materialia* **2019**, *5*, 100212. [[CrossRef](#)]
65. Park, J.S.; Mahmud, I.; Shin, H.J.; Park, M.K.; Ranjkesh, A.; Lee, D.K.; Kim, H.R. Effect of Surface Energy and Seed Layer Annealing Temperature on ZnO Seed Layer Formation and ZnO Nanowire Growth. *Appl. Surf. Sci.* **2016**, *362*, 132–139. [[CrossRef](#)]
66. Demes, T.; Ternon, C.; Riassetto, D.; Stambouli, V.; Langlet, M. Comprehensive Study of Hydrothermally Grown ZnO Nanowires. *J. Mater. Sci.* **2016**, *51*, 10652–10661. [[CrossRef](#)]
67. Song, J.; Lim, S. Effect of Seed Layer on the Growth of ZnO Nanorods. *J. Phys. Chem. C* **2007**, *111*, 596–600. [[CrossRef](#)]
68. Nirmal Peiris, T.A.; Alessa, H.; Sagu, J.S.; Ahmad Bhatti, I.; Isherwood, P.; Upul Wijayantha, K.G. Effect of ZnO Seed Layer Thickness on Hierarchical ZnO Nanorod Growth on Flexible Substrates for Application in Dye-Sensitised Solar Cells. *J. Nanoparticle Res.* **2013**, *15*. [[CrossRef](#)]
69. Nur, M.; Ghazali, I.; Ammar, M.; Nor, S.; Mustaffa, A.; Abubakar, S.; Husham, M.; Sagadevan, S.; Paiman, S. A Comparative Approach on One-Dimensional ZnO Nanowires for Morphological and Structural Properties. *J. Cryst. Growth* **2021**, *558*, 125997. [[CrossRef](#)]
70. Wu, W.Y.; Yeh, C.C.; Ting, J.M. Effects of Seed Layer Characteristics on the Synthesis of ZnO Nanowires. *J. Am. Ceram. Soc.* **2009**, *92*, 2718–2723. [[CrossRef](#)]
71. Cheng, J.J.; Nicaise, S.M.; Berggren, K.K.; Gradečak, S. Dimensional Tailoring of Hydrothermally Grown Zinc Oxide Nanowire Arrays. *Nano Lett.* **2016**, *16*, 753–759. [[CrossRef](#)]
72. Cossuet, T.; Roussel, H.; Chauveau, J.M.; Chaix-Pluchery, O.; Thomassin, J.L.; Appert, E.; Consonni, V. Well-Ordered ZnO Nanowires with Controllable Inclination on Semipolar ZnO Surfaces by Chemical Bath Deposition. *Nanotechnology* **2018**, *29*, 475601. [[CrossRef](#)]
73. Alshehri, N.A.; Lewis, A.R.; Pleydell-Pearce, C.; Maffei, T.G.G. Investigation of the Growth Parameters of Hydrothermal ZnO Nanowires for Scale up Applications. *J. Saudi Chem. Soc.* **2018**, *22*, 538–545. [[CrossRef](#)]
74. Liu, Q.; Yasui, T.; Nagashima, K.; Yanagida, T.; Hara, M.; Horiuchi, M.; Zhu, Z.; Takahashi, H.; Shimada, T.; Arima, A.; et al. Ammonia-Induced Seed Layer Transformations in a Hydrothermal Growth Process of Zinc Oxide Nanowires. *J. Phys. Chem. C* **2020**, *124*, 20563–20568. [[CrossRef](#)]
75. Yi, Z.; Luo, J.; Ye, X.; Yi, Y.; Huang, J.; Yi, Y.; Duan, T.; Zhang, W.; Tang, Y. Effect of Synthesis Conditions on the Growth of Various ZnO Nanostructures and Corresponding Morphology-Dependent Photocatalytic Activities. *Superlattices Microstruct.* **2016**, *100*, 907–917. [[CrossRef](#)]
76. Abdulrahman, A.F.; Ahmed, S.M.; Hamad, S.M.; Almessiere, M.A.; Ahmed, N.M.; Sajadi, S.M. Effect of Different PH Values on Growth Solutions for the ZnO Nanostructures. *Chinese J. Phys.* **2021**, *71*, 175–189. [[CrossRef](#)]
77. Rayerfrancis, A.; Balaji Bhargav, P.; Ahmed, N.; Chandra, B.; Dhara, S. Effect of PH on the Morphology of ZnO Nanostructures and Its Influence on Structural and Optical Properties. *Phys. B Condens. Matter* **2015**, *457*, 96–102. [[CrossRef](#)]
78. Muchuweni, E.; Sathiaraj, T.S.; Nyakoty, H. Effect of Annealing on the Microstructural, Optical and Electrical Properties of ZnO Nanowires by Hydrothermal Synthesis for Transparent Electrode Fabrication. *Mater. Sci. Eng. B Solid-State Mater. Adv. Technol.* **2018**, *227*, 68–73. [[CrossRef](#)]
79. Speirs, M.J.; Dirin, D.N.; Abdu-Aguye, M.; Balazs, D.M.; Kovalenko, M.V.; Loi, M.A. Temperature Dependent Behaviour of Lead Sulfide Quantum Dot Solar Cells and Films. *Energy Environ. Sci.* **2016**, *9*, 2916–2924. [[CrossRef](#)]
80. Nelson, J.A. *The Physics of Solar Cells*; World Scientific Publishing Company: Singapore, 2003; ISBN 1848168233.
81. Clifford, J.P.; Johnston, K.W.; Levina, L.; Sargent, E.H. Schottky Barriers to Colloidal Quantum Dot Films. *Appl. Phys. Lett.* **2007**, *91*, 253117. [[CrossRef](#)]
82. Kramer, I.J.; Sargent, E.H. The Architecture of Colloidal Quantum Dot Solar Cells: Materials to Devices. *Chem. Rev.* **2014**, *114*, 863–882. [[CrossRef](#)] [[PubMed](#)]
83. Leschkies, K.S.; Jacobs, A.G.; Norris, D.J.; Aydil, E.S. Nanowire-Quantum-Dot Solar Cells and the Influence of Nanowire Length on the Charge Collection Efficiency. *Appl. Phys. Lett.* **2009**, *95*, 1–4. [[CrossRef](#)]
84. Jean, J.; Chang, S.; Brown, P.R.; Cheng, J.J.; Rekemeyer, P.H.; Bawendi, M.G.; Gradecak, S.; Bulovic, V. ZnO Nanowire Arrays for Enhanced Photocurrent in PbS Quantum Dot Solar Cells. *Adv. Mater.* **2013**, *25*, 2790–2796. [[CrossRef](#)] [[PubMed](#)]
85. Wang, H.; Kubo, T.; Nakazaki, J.; Kinoshita, T.; Segawa, H. PbS-Quantum-Dot-Based Heterojunction Solar Cells Utilizing ZnO Nanowires for High External Quantum Efficiency in the near-Infrared Region. *J. Phys. Chem. Lett.* **2013**, *4*, 2455–2460. [[CrossRef](#)]
86. Chang, J.; Kuga, Y.; Mora-Seró, I.; Toyoda, T.; Ogomi, Y.; Hayase, S.; Bisquert, J.; Shen, Q. High Reduction of Interfacial Charge Recombination in Colloidal Quantum Dot Solar Cells by Metal Oxide Surface Passivation. *Nanoscale* **2015**, *7*, 5446–5456. [[CrossRef](#)]
87. Kawawaki, T.; Wang, H.; Kubo, T.; Saito, K.; Nakazaki, J.; Segawa, H.; Tatsuma, T. Efficiency Enhancement of PbS Quantum Dot/ZnO Nanowire Bulk-Heterojunction Solar Cells by Plasmonic Silver Nanocubes. *ACS Nano* **2015**, *9*, 4165–4172. [[CrossRef](#)]
88. Wang, H.; Gonzalez-Pedro, V.; Kubo, T.; Fabregat-Santiago, F.; Bisquert, J.; Sanehira, Y.; Nakazaki, J.; Segawa, H. Enhanced Carrier Transport Distance in Colloidal PbS Quantum-Dot-Based Solar Cells Using ZnO Nanowires. *J. Phys. Chem. C* **2015**, *119*, 27265–27274. [[CrossRef](#)]
89. Zang, S.; Wang, Y.; Su, W.; Zhu, H.; Li, G.; Zhang, X.; Liu, Y. Increased Open-Circuit Voltage of ZnO Nanowire/PbS Quantum Dot Bulk Heterojunction Solar Cells with Solution-Deposited Mg(OH)₂ Interlayer. *Phys. Status Solidi Rapid Res. Lett.* **2016**, *10*, 745–748. [[CrossRef](#)]

90. Wang, H.; Kubo, T.; Nakazaki, J.; Segawa, H. Solution-Processed Short-Wave Infrared PbS Colloidal Quantum Dot/ZnO Nanowire Solar Cells Giving High Open-Circuit Voltage. *ACS Energy Lett.* **2017**, *2*, 2110–2117. [[CrossRef](#)]
91. Cheng, J.J.; Chuang, C.H.M.; Hentz, O.; Rekemeyer, P.H.; Bawendi, M.G.; Gradečak, S. Dimension- and Surface-Tailored ZnO Nanowires Enhance Charge Collection in Quantum Dot Photovoltaic Devices. *ACS Appl. Energy Mater.* **2018**, *1*, 1815–1822. [[CrossRef](#)]
92. Ozu, S.; Zhang, Y.; Yasuda, H.; Kitabatake, Y.; Toyoda, T.; Hirata, M.; Yoshino, K.; Katayama, K.; Hayase, S.; Wang, R.; et al. Improving Photovoltaic Performance of ZnO Nanowires Based Colloidal Quantum Dot Solar Cells via SnO₂ Passivation Strategy. *Front. Energy Res.* **2019**, *7*, 11. [[CrossRef](#)]
93. Tavakoli Dastjerdi, H.; Prochowicz, D.; Yadav, P.; Tavakoli, M.M. Tuning Areal Density and Surface Passivation of ZnO Nanowire Array Enable Efficient PbS QDs Solar Cells with Enhanced Current Density. *Adv. Mater. Interfaces* **2020**, *7*, 1–9. [[CrossRef](#)]
94. Lan, X.; Voznyy, O.; Kiani, A.; García de Arquer, F.P.; Abbas, A.S.; Kim, G.; Liu, M.; Yang, Z.; Walters, G.; Xu, J. Passivation Using Molecular Halides Increases Quantum Dot Solar Cell Performance. *Adv. Mater.* **2016**, *28*, 299–304. [[CrossRef](#)]
95. Zhitomirsky, D.; Voznyy, O.; Hoogland, S.; Sargent, E.H. Measuring Charge Carrier Diffusion in Coupled Colloidal Quantum Dot Solids. *ACS Nano* **2013**, *7*, 5282–5290. [[CrossRef](#)]
96. Kramer, I.J.; Zhitomirsky, D.; Bass, J.D.; Rice, P.M.; Topuria, T.; Krupp, L.; Thon, S.M.; Ip, A.H.; Debnath, R.; Kim, H.C.; et al. Ordered Nanopillar Structured Electrodes for Depleted Bulk Heterojunction Colloidal Quantum Dot Solar Cells. *Adv. Mater.* **2012**, *24*, 2315–2319. [[CrossRef](#)]
97. Carey, G.H.; Levina, L.; Comin, R.; Voznyy, O.; Sargent, E.H. Record Charge Carrier Diffusion Length in Colloidal Quantum Dot Solids via Mutual Dot-to-Dot Surface Passivation. *Adv. Mater.* **2015**, *27*, 3325–3330. [[CrossRef](#)]
98. Sharma, A.; Mahajan, C.; Rath, A.K. Reduction of Trap and Polydispersity in Mutually Passivated Quantum Dot Solar Cells. *ACS Appl. Energy Mater.* **2020**, *3*, 8903–8911. [[CrossRef](#)]
99. Wang, Y.; Lu, K.; Han, L.; Liu, Z.; Shi, G.; Fang, H.; Chen, S.; Wu, T.; Yang, F.; Gu, M.; et al. In Situ Passivation for Efficient PbS Quantum Dot Solar Cells by Precursor Engineering. *Adv. Mater.* **2018**, *30*, 1–8. [[CrossRef](#)] [[PubMed](#)]
100. Ip, A.H.; Thon, S.M.; Hoogland, S.; Voznyy, O.; Zhitomirsky, D.; Debnath, R.; Levina, L.; Rollny, L.R.; Carey, G.H.; Fischer, A.; et al. Hybrid Passivated Colloidal Quantum Dot Solids. *Nat. Nanotechnol.* **2012**, *7*, 577–582. [[CrossRef](#)]
101. Vempati, S.; Mitra, J.; Dawson, P. One-Step Synthesis of ZnO Nanosheets: A Blue-White Fluorophore. *Nanoscale Res. Lett.* **2012**, *7*, 1–10. [[CrossRef](#)]
102. Zhang, X.; Qin, J.; Xue, Y.; Yu, P.; Zhang, B.; Wang, L.; Liu, R. Effect of Aspect Ratio and Surface Defects on the Photocatalytic Activity of ZnO Nanorods. *Sci. Rep.* **2014**, *4*, 4–11. [[CrossRef](#)]
103. Ding, C.; Zhang, Y.; Liu, F.; Kitabatake, Y.; Hayase, S.; Toyoda, T.; Wang, R.; Yoshino, K.; Minemoto, T.; Shen, Q. Understanding Charge Transfer and Recombination by Interface Engineering for Improving the Efficiency of PbS Quantum Dot Solar Cells. *Nanoscale Horizons* **2018**, *3*, 417–429. [[CrossRef](#)]
104. Zhang, Y.; Ozu, S.; Wu, G.; Ding, C.; Liu, F.; Liu, D.; Minemoto, T.; Masuda, T.; Hayase, S.; Toyoda, T.; et al. In-Depth Exploration of the Charge Dynamics in Surface-Passivated ZnO Nanowires. *J. Phys. Chem. C* **2020**, *124*, 15812–15817. [[CrossRef](#)]
105. Tam, K.H.; Cheung, C.K.; Leung, Y.H.; Djuris, A.B.; Fung, S.; Kwok, W.M.; Chan, W.K.; Phillips, D.L.; Ding, L.; Ge, W.K. Defects in ZnO Nanorods Prepared by a Hydrothermal Method. *J. Phys. Chem. B* **2006**, *110*, 20865–20871. [[CrossRef](#)]
106. Xu, S.; Cheng, C.; Guo, W.; He, Y.; Huang, R.; Du, S.; Wang, N. Tuning the Optical and Electrical Properties of Hydrothermally Grown ZnO Nanowires by Sealed Post Annealing Treatment. *Solid State Commun.* **2013**, *160*, 41–46. [[CrossRef](#)]
107. Kim, W.; Kwak, G.; Jung, M.; Jo, S.K.; Miller, J.B.; Gellman, A.J.; Yong, K. Surface and Internal Reactions of ZnO Nanowires: Etching and Bulk Defect Passivation by H Atoms. *J. Phys. Chem. C* **2012**, *116*, 16093–16097. [[CrossRef](#)]
108. Xing, M.; Wei, Y.; Wang, R.; Zhang, Z. Study on the Performance of ZMO/PbS Quantum Dot Heterojunction Solar Cells. *Sol. Energy* **2021**, *213*, 53–58. [[CrossRef](#)]
109. Chen, Q.; Ding, H.; Wu, Y.; Sui, M.; Lu, W.; Wang, B.; Su, W.; Cui, Z.; Chen, L. Passivation of Surface States in the ZnO Nanowire with Thermally Evaporated Copper Phthalocyanine for Hybrid Photodetectors. *Nanoscale* **2013**, *5*, 4162–4165. [[CrossRef](#)]
110. Albaladejo-Siguan, M.; Baird, E.C.; Becker-Koch, D.; Li, Y.; Rogach, A.L.; Vaynzof, Y. Stability of Quantum Dot Solar Cells: A Matter of (Life)Time. *Adv. Energy Mater.* **2021**, *11*, 2003457. [[CrossRef](#)]